

Supporting Information

Dual-Reaction-Centre Enabled Concurrent N–C–N coupling for Effective Urea Electrosynthesis

Junxian Liu,^a Sean C. Smith,^b Xin Tan, ^{*c} YuanTong Gu,^a and Liangzhi Kou^{*a}

^a School of Mechanical, Medical and Process Engineering, Queensland University of Technology, Brisbane, QLD 4001, Australia. E-mail: liangzhi.kou@qut.edu.au

^b Integrated Materials Design Laboratory, Department of Materials Physics, Research School of Physics, The Australian National University, Australian Capital Territory, Canberra, ACT 2601, Australia.

^c Institute for Carbon Neutralization Technology, College of Chemistry and Materials Engineering, Wenzhou University, Wenzhou, Zhejiang 325035, P. R. China. E-mail: xintan@wzu.edu.cn

Computational Details

DFT computations. We perform spin-polarized DFT calculations within the Vienna Ab initio Simulation Package (VASP).¹ The ion-electron interactions are described with the projector-augmented wave pseudopotential (PAW).^{2,3} The electron exchange-correlation energy is calculated by Perdew-Burke-Ernzerhof (PBE) functional at the generalized gradient approximation (GGA) level.⁴ A 520 eV cutoff energy for the plane-wave basis is adopted in all the computations. The convergence criteria for the electronic self-consistent loop and the Hellmann-Feynman forces are set to be less than 10^{-5} eV and 0.01 eV/Å, respectively. The Brillouin zones are sampled using the Monkhorst-Pack mesh with a reciprocal space resolution of $2\pi \times 0.03 \text{ Å}^{-1}$ for structural optimization and $2\pi \times 0.01 \text{ Å}^{-1}$ for electronic properties calculations. A Gaussian smearing is employed with a smearing width of 0.05 eV. To prevent the artifactual interaction between periodical cells, a vacuum layer of 20 Å is applied along the z-direction. Grimme's D3 correction is adopted to describe the long-range van der Waals (vdW) interactions here.⁵⁻⁹ The computational results are subsequently post-processed using the VASPKIT code.¹⁰ To calculate the transition states and kinetic barriers of the key reaction step, the climbing image nudged elastic band (CI-NEB) approach is used with the force convergence of 0.03 eV/Å.^{11, 12} The AIMD simulations are performed using the NVT ensemble at 300 K for 20 ps.¹³ The aqueous environment is modeled as a continuum dielectric by the Poisson-Boltzmann implicit solvation using VASPsol code with a relative permittivity of 80.^{14, 15}

The cohesive energy of $\text{PcTM}_1\text{-O}_8\text{-TM}_2$ is defined as

$$E_{\text{coh}} = E_{\text{tot}} - 32E_{\text{C}} - 8E_{\text{O}} - 8E_{\text{N}} - 8E_{\text{H}} - E_{\text{TM}_1} - 2E_{\text{TM}_2} \quad (\text{S1})$$

where E_{tot} is the total energy of $\text{PcTM}_1\text{-O}_8\text{-TM}_2$, E_{TM_1} and E_{TM_2} are the energies of the metal atoms in their bulk phase. E_{C} , E_{O} , E_{N} , and E_{H} represent the energies of C, O, N, H atoms in their stable solid or gas phases.

Free energy computations. The free energy change for each electrochemical elementary reaction step (ΔG) is calculated following the computational hydrogen electrode (CHE) model developed by Nørskov et al.,^{16, 17} according to which the ΔG is evaluated as:

$$\Delta G = \Delta E + \Delta E_{\text{ZPE}} - T\Delta S + \Delta G_{\text{U}} + \Delta G_{\text{pH}} \quad (\text{S2})$$

where ΔE is the DFT computed reaction energy, ΔE_{ZPE} and ΔS are the differences between the adsorbed species and the gas phase in zero-point energy and entropy, respectively. T is the temperature of 298.15 K in our work. For adsorbed reaction intermediates, their E_{ZPE} and TS are obtained through

vibrational frequencies computations, while for molecules these values are taken from the NIST database. The specific values for E_{ZPE} and TS involved in this work are provided in Tables S5-9. ΔG_{U} and ΔG_{pH} are the effects of the applied electrode potential U and H^+ concentration, which can be determined as $-eU$ and $-k_{\text{B}}T \ln 10 \times \text{pH}$, respectively, where k_{B} is Boltzmann constant and the value of pH is assumed to be zero in a highly acidic solution.

Constant potential method. To more realistically simulate the influence of the experimental reaction condition on the intrinsic selectivity activity of $\text{PcV-O}_8\text{-Mn}$, the constant-potential method is adopted.^{18, 19} The aqueous environment is modeled using the implicit solvation approach with a relative permittivity of 80 by VASPsol code, in combination with explicit water molecules to better reflect solvation effects. Specifically, three randomly distributed H_2O molecules are incorporated as explicit water clusters, as previous studies have demonstrated that this solvation model provides a favorable balance between computational cost and accuracy, yielding more reliable results compared to models with more explicit water molecules.²⁰⁻²² The charges for each system are added from -1.0 e to $+1.0\text{ e}$ in steps of 0.5 e to clarify the electrode potential function. The potential dependent energy (E_{q}) of the catalysts can be calculated as:

$$E_{\text{q}} = E_{\text{scf}} + E_{\text{corr}} - q\phi_{\text{q}} \quad (\text{S3})$$

where E_{scf} is the self-consistent energy of DFT calculations, E_{corr} is the correction energy of the homogeneous background charge, q is the added number of electrons, and $-\phi_{\text{q}}$ is the work function of the charged slab. E_{corr} is the correction energy of background charge and is obtained by the average electrostatic potential of the systems $\langle \overline{V}_{\text{tot}} \rangle$:

$$E_{\text{corr}} = \int_0^q \langle \overline{V}_{\text{tot}} \rangle dQ \quad (\text{S4})$$

The electrode potential (U_{q}) of the charged systems referenced to the standard hydrogen electrode (SHE) is calculated as

$$U_{\text{q}} = -4.6 - \phi_{\text{q}} / eV \quad (\text{S5})$$

where 4.6 V is the work function of the H_2/H^+ couple at standard conditions. The energy varies with the electrode potential as a quadratic function, which takes the form

$$E(U_{\text{q}}) = -\frac{1}{2}C(U_{\text{q}} - U_0)^2 + E_0 \quad (\text{S6})$$

where C is the capacitance of the system, U_0 is the potential of zero charges (PZC), and E_0 is the energy at the zero charges.

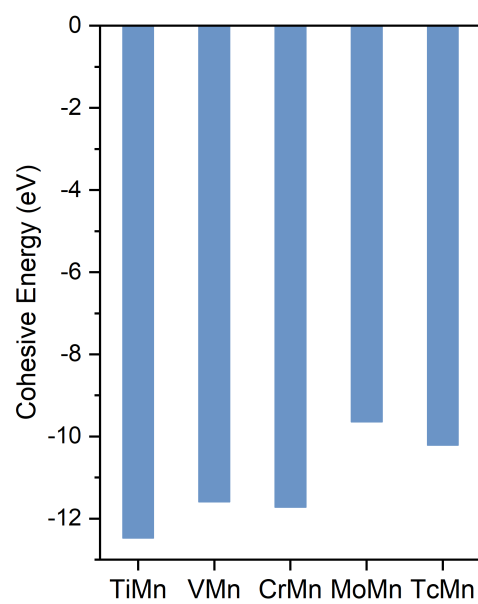


Figure S1. Cohesive energy of PcTM-O₈-Mn (TM = Ti, V, Cr, Mo, and Tc).

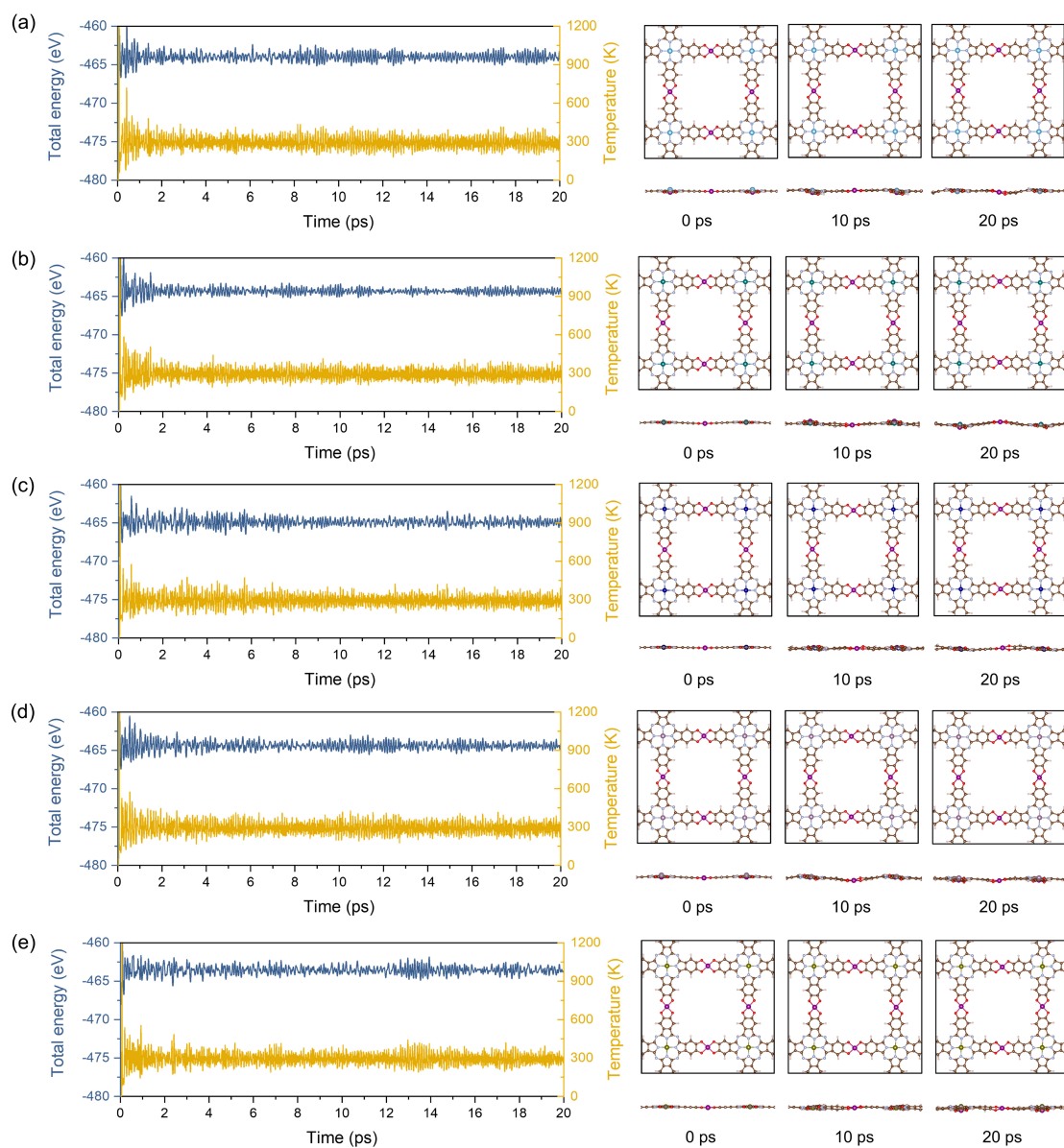


Figure S2. Variations of temperature and energy against time from AIMD simulations for PcTM-O₈-Mn. (a) PcTi-O₈-Mn, (b) PcV-O₈-Mn, (c) PcCr-O₈-Mn, (d) PcMo-O₈-Mn, and (e) PcTc-O₈-Mn. Right panels are structure snapshots of PcTM-O₈-Mn at 300 K after 10 ps and 20 ps AIMD simulations, respectively.

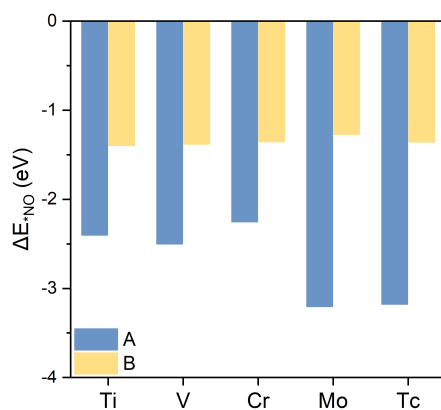


Figure S3. Adsorption energies of NO (ΔE_{NO}^*) on the A and B sites of PcTM-O₈-Mn.

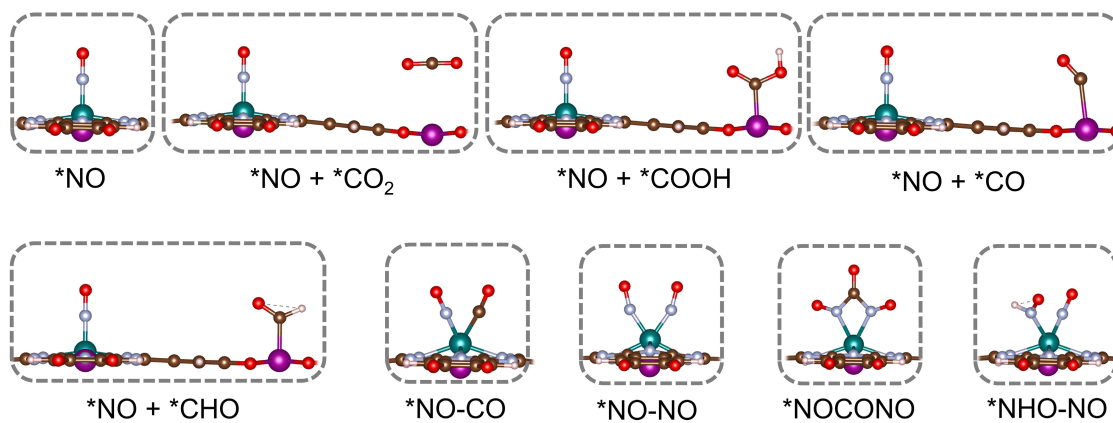


Figure S4. Side view of the atomic structures of optimized reaction intermediates involved in the synchronous NO activation and CO₂ reduction process on PcV-O₈-Mn.

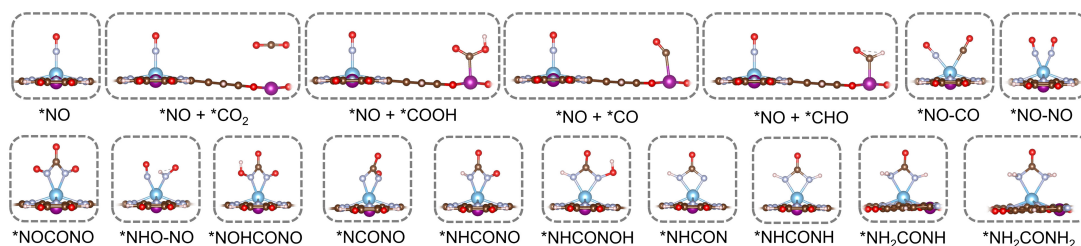


Figure S6. Side view of all optimized reaction intermediates throughout the urea formation process on PcTi-O₈-Mn.

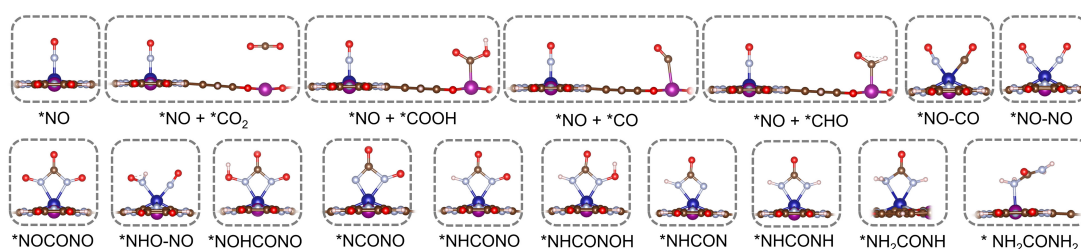


Figure S7. Side view of all optimized reaction intermediates throughout the urea formation process on PcCr-O₈-Mn.

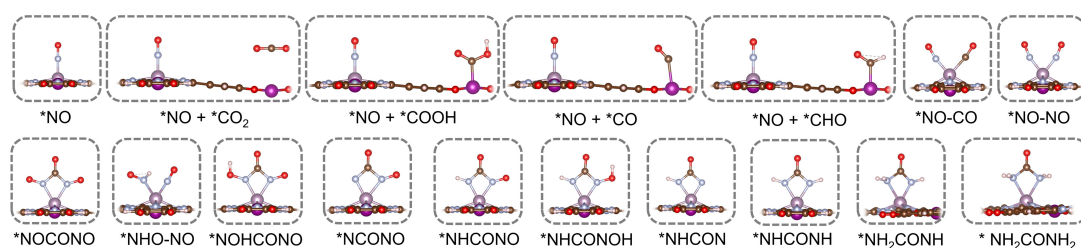


Figure S8. Side view of all optimized reaction intermediates throughout the urea formation process on PcMo-O₈-Mn.

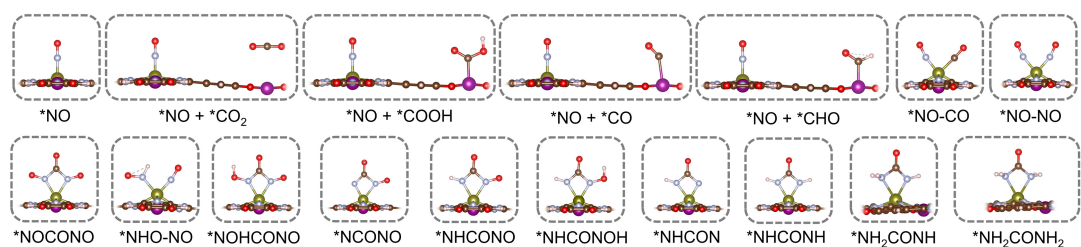


Figure S9. Side view of all optimized reaction intermediates throughout the urea formation process on PcTc-O₈-Mn.

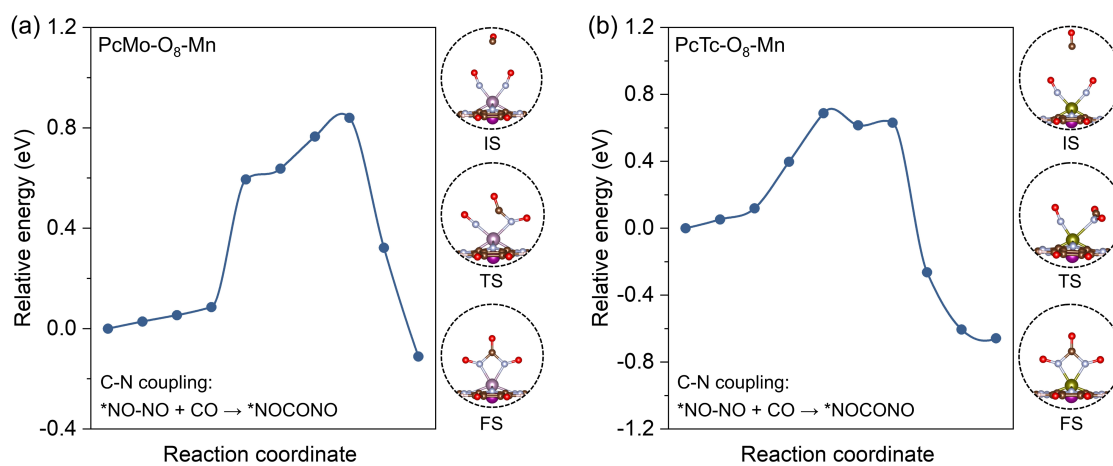


Figure S10. Kinetic energy barriers for N-C-N bond formation on (a) PcMo-O₈-Mn and (b) PcTc-O₈-Mn.

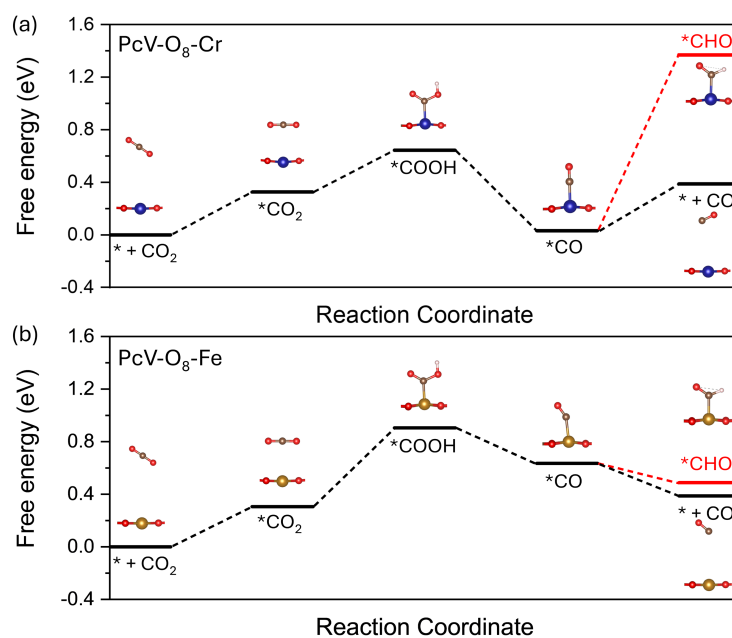


Figure S11. Free energy profiles of electrochemical CO₂ reduction on (a) Cr at PcV-O₈-Cr and (b) Fe at PcV-O₈-Fe.

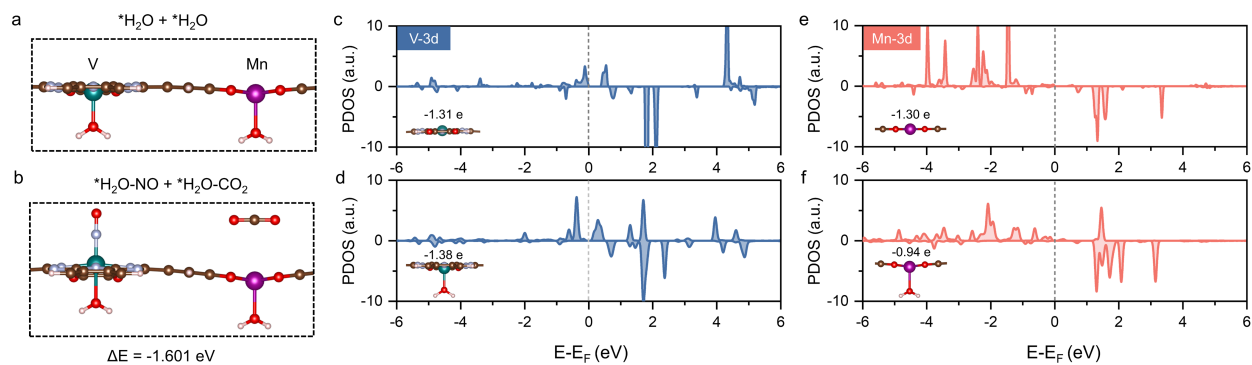


Figure S12. Side view of the optimized structures of (a) $^*\text{H}_2\text{O} + ^*\text{H}_2\text{O}$ and (b) $^*\text{H}_2\text{O-NO} + ^*\text{H}_2\text{O-CO}_2$ on $\text{PcV-O}_8\text{-Mn}$ with two pre-adsorbed water molecules. PDOS of the V and Mn 3d orbitals for $\text{PcV-O}_8\text{-Mn}$: (c) and (e) without pre-adsorbed water molecules; (d) and (f) with two pre-adsorbed water molecules.

Note 1: Construction of Pourbaix Diagrams. The Pourbaix diagram reveals the thermodynamically stable structures in electrochemical systems as a function of pH and applied electrode potential (U_{SHE}).²³⁻²⁷ In this study, we constructed the Pourbaix diagrams for 2D PcTM-O₈-Mn by calculating the free-energy changes for possible adsorption species, that is, *O and *OH. For both adsorbates, each reaction can be written as follows:



Then, free energy change (ΔG) for *O and *OH species were calculated at zero potential and standard conditions to obtain following equations:

$$\Delta G_{*O} = G_{*O} + G_{\text{H}_2} - G^* - G_{\text{H}_2\text{O}} \quad (\text{S9})$$

$$\Delta G_{*OH} = G_{*OH} + 0.5G_{\text{H}_2} - G^* - G_{\text{H}_2\text{O}} \quad (\text{S10})$$

Therefore, the ΔG for *O and *OH species as a function of pH and U can be defined as follows at 298.15 K:

$$\Delta G(\text{pH}, U) = \Delta G - v(\text{H}^+) \cdot k_B T \cdot \ln 10 \cdot \text{pH} - v(\text{e}^-) \cdot e \cdot U \quad (\text{S11})$$

where k_B is the Boltzmann constant and the value of $k_B T \cdot \ln 10$ is 0.059; $v(\text{H}^+)$, and $v(\text{e}^-)$ are values for the stoichiometric coefficients of transferred protons and electrons of corresponding adsorption processes (Equations S1-2), respectively. And U denotes the applied electrode potential referenced to standard hydrogen electrode (SHE).

By applying pH and U, the ΔG can be rewritten as follows:

$$\begin{aligned} \Delta G_{*O}(\text{pH}, U) &= \Delta G_{O^*} - 2(0.059 \cdot \text{pH}) - 2eU \\ &= \Delta G_{O^*} - 0.118 \cdot \text{pH} - 2eU \end{aligned} \quad (\text{S12})$$

$$\Delta G_{*OH}(\text{pH}, U) = \Delta G_{OH^*} - 0.059 \cdot \text{pH} - eU \quad (\text{S13})$$

At pH = 0, ΔG for all species as a function of U were initially adopted to determine the phase boundaries. Subsequently, the effect of pH is applied to finally construct the Pourbaix diagrams for 2D PcTM-O₈-Mn.

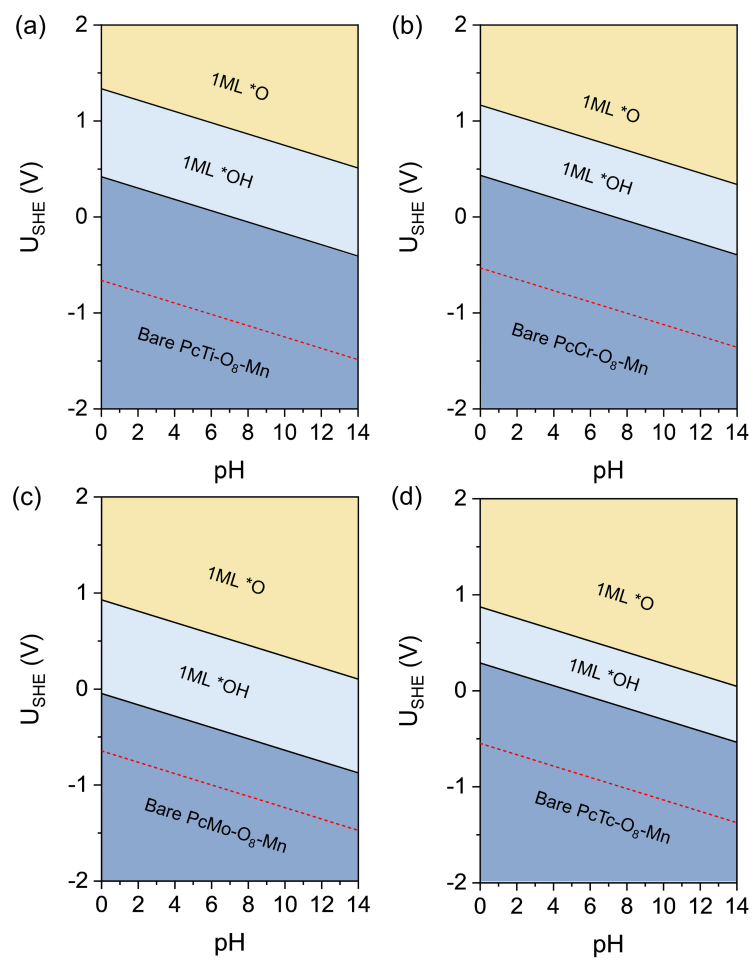


Figure S13. Surface Pourbaix diagram of (a) PcTi-O₈-Mn, (b) PcCr-O₈-Mn, (c) PcMo-O₈-Mn, and (d) PcTc-O₈-Mn.

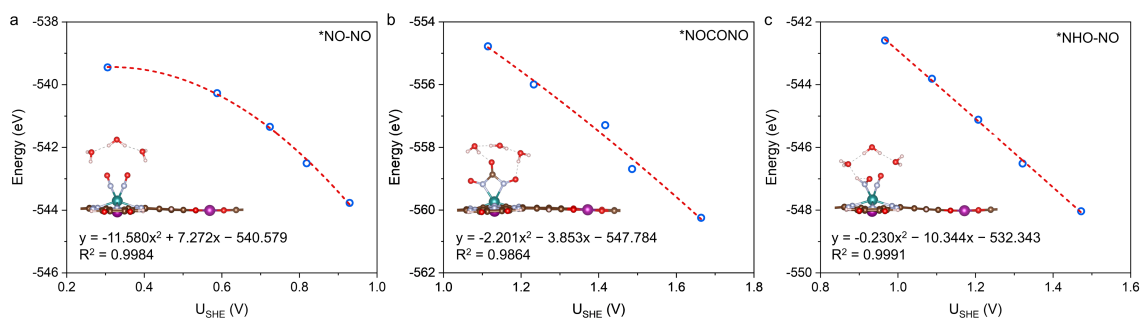


Figure S14. The potential versus free energy of (a) *NO-NO, (b) *NOCONO, and (c) *NHO-NO intermediates on PcV-O₈-Mn with a H₆O₃ cluster.

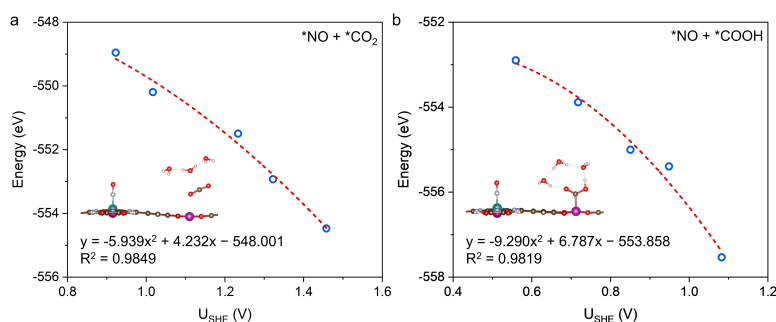


Figure S15. The potential versus free energy of (a) *NO + *CO₂ and (b) *NO + *COOH intermediates on PcV-O₈-Mn with a H₆O₃ cluster.

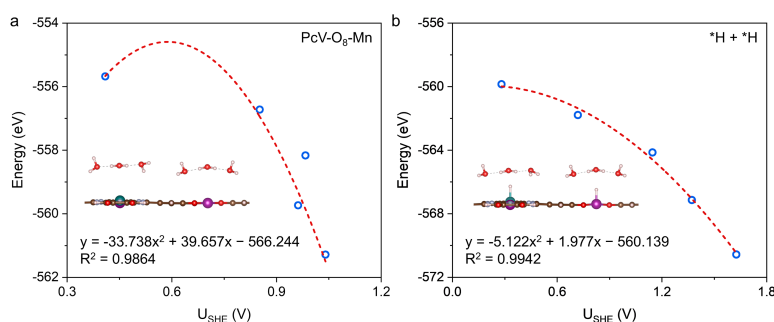


Figure S16. The potential versus free energy of (a) the pure surface and (b) *H + *H intermediate on PcV-O₈-Mn with two H₆O₃ clusters.

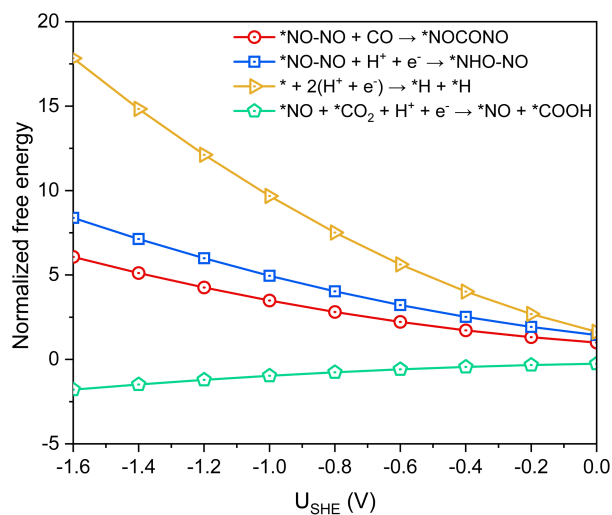


Figure S17. Normalized free energies of the *NO + *COOH formation, N–C–N coupling, *NO-NO hydrogenation, and HER steps on PcV-O₈-Mn surface as a function of the applied electrode potential vs standard hydrogen electrode. All reaction free energies are referenced to the N–C–N coupling step at 0 V.

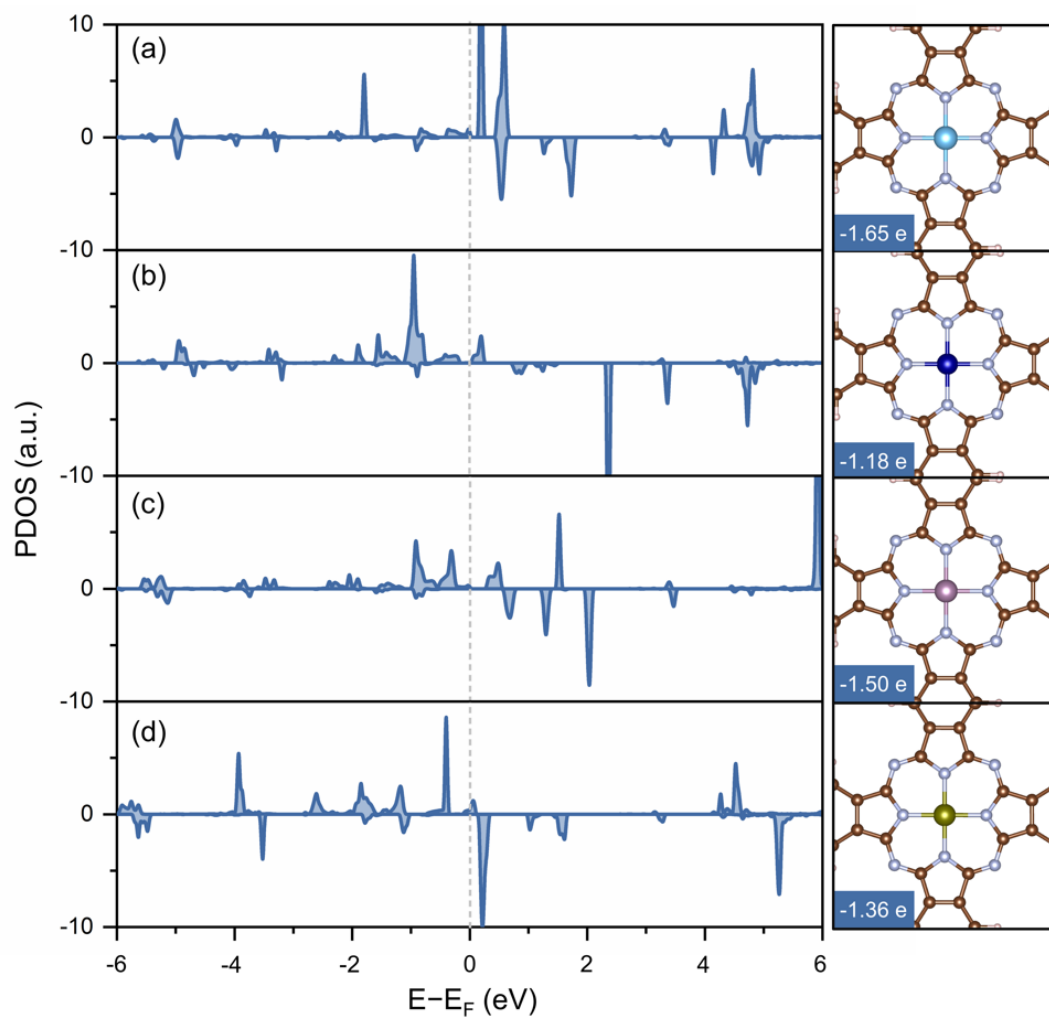


Figure S18. Partial density of states (PDOS) for (a) Ti d orbitals of PcTi-O₈-Mn, (b) Cr d orbitals of PcCr-O₈-Mn, (c) Mo d orbitals of PcMo-O₈-Mn, and (d) Tc d orbitals of PcTc-O₈-Mn.

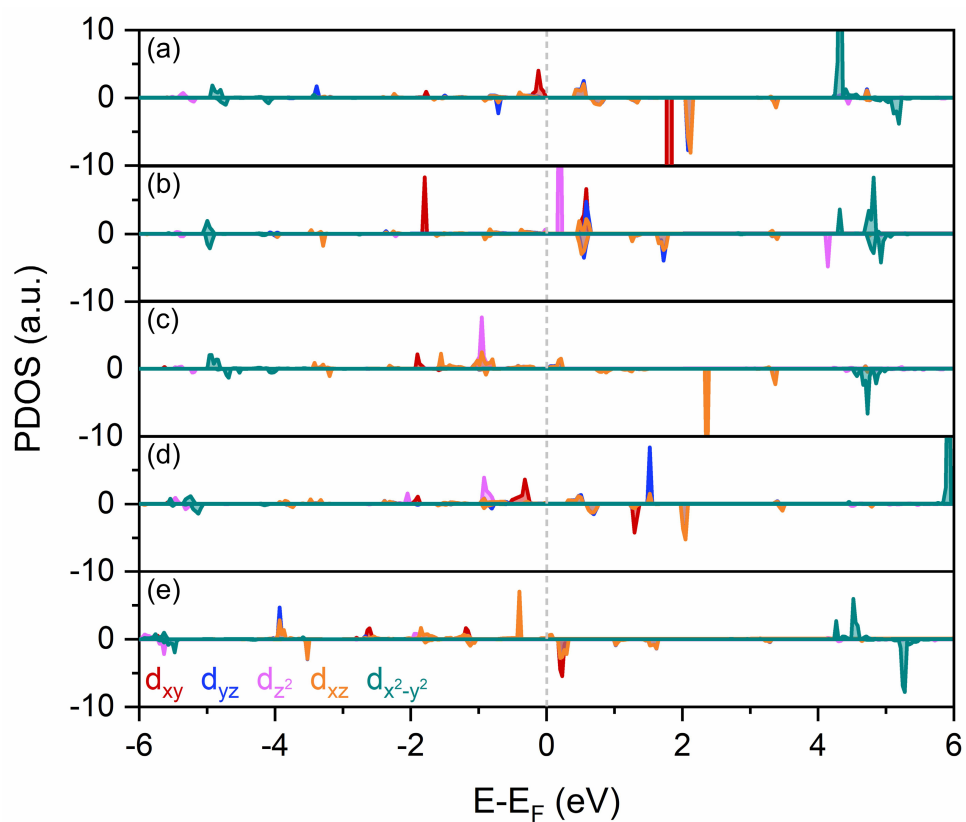
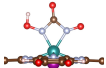
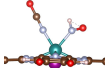
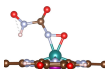
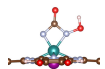
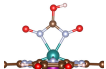
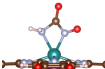
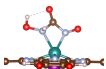
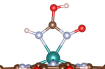
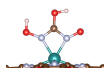
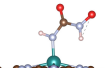
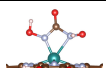
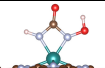
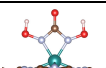
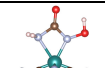
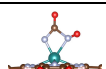
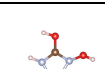
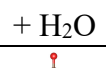
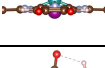
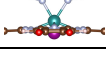
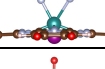


Figure S19. Partial density of states (PDOS) for each d orbital of (a) V in PcV-O₈-Mn, (b) Ti in PcTi-O₈-Mn, (c) Cr in PcCr-O₈-Mn, (d) Mo in PcMo-O₈-Mn, and (e) Tc in PcTc-O₈-Mn.

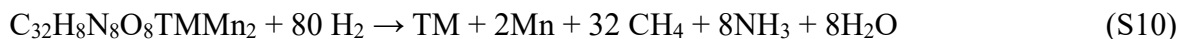
Table S1. The reaction free energies (ΔG) of possible competing reactions during the urea formation process on PcTM-O₈-Mn (TM = Ti, V, Cr, Mo, and Tc). Bold fonts represent thermodynamically feasible reactions.

Competing reactions		Ti	V	Cr	Mo	Tc
1	$*NO + *CO \rightarrow *NO + CO$	-0.26	-0.25	-0.36	-0.24	-0.22
	$*NO + *CO + H^+ + e^- \rightarrow *NO + *CHO$	-0.01	0.02	-0.06	0.03	0.01
2	$*NO + NO \rightarrow *NO-NO$	-0.59	-0.12	0.16	-0.95	-0.19
	$*NO + CO \rightarrow *NO-CO$	0.65	0.47	1.25	0.46	0.29
3	$*NO-NO + CO \rightarrow *NOCONO$	-0.46	-0.40	0.26	0.45	0.16
	$*NO-NO + H^+ + e^- \rightarrow *NHO-NO$	0.39	0.03	0.63	0.61	0.17

Table S2. Competitive intermediates during the whole reduction pathway for PcV-O₈-Mn. (Bold fonts denote the energetically favorable species, and numbers in brackets indicate the reaction free energies.)

Step	Configuration	E (eV)	Step	Configuration	E (eV)
1 st		-516.125	3 rd		-510.274
		-515.975			-510.012
		-516.002	4 th		-514.655
2 nd		-519.735			-514.726
		-519.674			-514.528
		-519.432			-515.027
		-520.239 (-0.349)	5 th		-519.221 (-0.459)
	 + H ₂ O	-505.809 (-0.961)			-518.652
3 rd		-510.740			-519.082
		-509.908		 + H ₂ O	-504.414 (-0.624)

Note 2: Thermodynamic Reduction Potentials of PcTM-O₈-Mn in Aqueous Solution. With reference to the componential analysis and the modified method mentioned in the previous literature,^{28,}²⁹ we assume the PcTM-O₈-Mn (C₃₂H₈N₈O₈TMMn₂) can be reduced by the electrons through the following reaction:



The thermodynamic reduction potential of PcTM-O₈-Mn (ϕ) could be calculated as following:

$$\phi = -[\Delta_f G^\circ(\text{TM}) + 2\Delta_f G^\circ(\text{Mn}) + 32\Delta_f G^\circ(\text{CH}_4) + 8\Delta_f G^\circ(\text{NH}_3) + \Delta_f G^\circ(\text{H}_2\text{O}) - \Delta_f G^\circ(\text{C}_{32}\text{H}_8\text{N}_8\text{O}_8\text{TMMn}_2) - 80\Delta_f G^\circ(\text{H}_2)]/160eF + \phi(\text{H}^+/\text{H}_2) \quad (\text{S11})$$

where $\Delta_f G^\circ(\text{TM})$, $\Delta_f G^\circ(\text{Mn})$, $\Delta_f G^\circ(\text{CH}_4)$, $\Delta_f G^\circ(\text{NH}_3)$, $\Delta_f G^\circ(\text{H}_2\text{O})$, and $\Delta_f G^\circ(\text{H}_2)$ are the standard molar Gibbs energies of formation for TM, Mn, CH₄, NH₃, H₂O, and H₂, respectively, as obtained from the handbook.³⁰ For the standard molar Gibbs formation energy of PcTM-O₈-Mn is approximated by its cohesive energy (E_{coh}). $\phi(\text{H}^+/\text{H}_2)$ is 0 V relative to the normal hydrogen electrode (NHE) potential. F and e represent the Faraday constant and the elemental charge, respectively. Based on Equation S11, ϕ values for are PcTM-O₈-Mn (TM = Ti, V, Cr, Mo, and Tc) obtained as about 0.10 V (relative to NHE), all higher than their U_L values, promising PcTM-O₈-Mn systems can be resistant against the electrochemical reduction conditions.

Table S3. Standard Molar Gibbs Energy of Formation ($\Delta_f G^\circ$, kJ/mol) at 298.15 K and thermodynamic reduction potential (ϕ , V) of the PcTM-O₈-Mn.

Molecular formula	$\Delta_f G^\circ$	Molecular formula	$\Delta_f G^\circ$	PcTM-O ₈ -Mn	ϕ
H ₂	0	V	754.4	Ti	0.10
H ₂ O	-237.1	Cr	351.8	V	0.08
CH ₄	-50.5	Mn	238.5	Cr	0.11
NH ₃	-16.4	Mo	612.5	Mo	0.10
Ti	428.4	Tc	678.0	Tc	0.10

Table S4. The reaction energies (ΔE , eV) of the last two gorgoneion steps for $^*\text{NH}_2\text{CONH}_2$ on $\text{VN}_3@\text{G}$, $\text{VN}_4\text{-py}@\text{G}$, and $\text{VN}_4\text{-pr}@\text{G}$.

Structures	$\Delta E (^*\text{NHCONH} \rightarrow ^*\text{NH}_2\text{CONH})$	$\Delta E (^*\text{NH}_2\text{CONH} \rightarrow ^*\text{NH}_2\text{CONH}_2)$
$\text{VN}_3@\text{G}$	-0.74	0.22
$\text{VN}_4\text{-py}@\text{G}$	-0.65	0.23
$\text{VN}_4\text{-pr}@\text{G}$	-1.22	-1.10

Table S5. The calculated values of ZPE (eV) and TS (eV) for all intermediates on $\text{PcV-O}_8\text{-Mn}$.

Intermediates	ZPE	TS	Intermediates	ZPE	TS
$^*\text{NO}$	0.20	0.14	$^*\text{NOHCONO}$	0.97	0.31
$^*\text{NO} + ^*\text{CO}_2$	0.52	0.34	$^*\text{NCONO}$	0.53	0.30
$^*\text{NO} + ^*\text{COOH}$	0.82	0.33	$^*\text{NHCONO}$	0.88	0.27
$^*\text{NO} + ^*\text{CO}$	0.37	0.34	$^*\text{NHCONOH}$	1.20	0.27
$^*\text{NO} + ^*\text{CHO}$	0.67	0.30	$^*\text{NHCON}$	0.78	0.19
$^*\text{NO-CO}$	0.41	0.26	$^*\text{NHCONH}$	1.10	0.21
$^*\text{NO-NO}$	0.39	0.21	$^*\text{NH}_2\text{CONH}$	1.46	0.23
$^*\text{NHO-NO}$	0.69	0.30	$^*\text{NH}_2\text{CONH}_2$	1.79	0.29
$^*\text{NOCONO}$	0.68	0.33			

Table S6. The calculated values of ZPE (eV) and TS (eV) for all intermediates on $\text{PcTi-O}_8\text{-Mn}$.

Intermediates	ZPE	TS	Intermediates	ZPE	TS
$^*\text{NO}$	0.17	0.17	$^*\text{NOHCONO}$	0.97	0.37
$^*\text{NO} + ^*\text{CO}_2$	0.50	0.35	$^*\text{NCONO}$	0.52	0.32
$^*\text{NO} + ^*\text{COOH}$	0.80	0.36	$^*\text{NHCONO}$	0.86	0.30
$^*\text{NO} + ^*\text{CO}$	0.35	0.35	$^*\text{NHCONOH}$	1.17	0.29
$^*\text{NO} + ^*\text{CHO}$	0.65	0.31	$^*\text{NHCON}$	0.73	0.25
$^*\text{NO-CO}$	0.37	0.33	$^*\text{NHCONH}$	1.09	0.22
$^*\text{NO-NO}$	0.39	0.25	$^*\text{NH}_2\text{CONH}$	1.45	0.24
$^*\text{NHO-NO}$	0.65	0.34	$^*\text{NH}_2\text{CONH}_2$	1.73	0.26
$^*\text{NOCONO}$	0.67	0.34			

Table S7. The calculated values of ZPE (eV) and TS (eV) for all intermediates on PcCr-O₈-Mn.

Intermediates	ZPE	TS	Intermediates	ZPE	TS
*NO	0.20	0.14	*NOHCONO	0.97	0.35
*NO + *CO ₂	0.53	0.33	*NCONO	0.56	0.26
*NO + *COOH	0.84	0.32	*NHCONO	0.87	0.28
*NO + *CO	0.38	0.26	*NHCONOH	1.18	0.29
*NO + *CHO	0.68	0.30	*NHCON	0.75	0.21
*NO-CO	0.41	0.29	*NHCONH	1.04	0.22
*NO-NO	0.43	0.26	*NH ₂ CONH	1.45	0.24
*NHO-NO	0.71	0.28	*NH ₂ CONH ₂	1.79	0.29
*NOCONO	0.67	0.33			

Table S8. The calculated values of ZPE (eV) and TS (eV) for all intermediates on PcMo-O₈-Mn.

Intermediates	ZPE	TS	Intermediates	ZPE	TS
*NO	0.20	0.12	*NOHCONO	0.98	0.33
*NO + *CO ₂	0.53	0.38	*NCONO	0.56	0.26
*NO + *COOH	0.83	0.32	*NHCONO	0.90	0.26
*NO + *CO	0.37	0.33	*NHCONOH	1.19	0.27
*NO + *CHO	0.68	0.29	*NHCON	0.78	0.19
*NO-CO	0.41	0.25	*NHCONH	1.09	0.22
*NO-NO	0.42	0.24	*NH ₂ CONH	1.46	0.23
*NHO-NO	0.71	0.29	*NH ₂ CONH ₂	1.76	0.24
*NOCONO	0.67	0.33			

Table S9. The calculated values of ZPE (eV) and TS (eV) for all intermediates on PcTc-O₈-Mn.

Intermediates	ZPE	TS	Intermediates	ZPE	TS
*NO	0.21	0.12	*NOHCONO	0.97	0.35
*NO + *CO ₂	0.54	0.33	*NCONO	0.56	0.26
*NO + *COOH	0.84	0.32	*NHCONO	0.89	0.27
*NO + *CO	0.38	0.34	*NHCONOH	1.16	0.30
*NO + *CHO	0.68	0.31	*NHCON	0.76	0.20
*NO-CO	0.43	0.20	*NHCONH	1.07	0.23
*NO-NO	0.43	0.26	*NH ₂ CONH	1.47	0.23
*NHO-NO	0.73	0.27	*NH ₂ CONH ₂	1.78	0.23
*NOCONO	0.68	0.32			

Table S10. The values of ZPE (eV) and TS (eV) for the gas-phase molecules.

Molecules	ZPE	TS
H ₂	0.27	0.41
H ₂ O	0.56	0.67
NO	0.12	0.65
CO ₂	0.31	0.65
CO	0.13	0.61

References

1. G. Kresse and J. Hafner, *Physical Review B*, 1993, **47**, 558.
2. P. E. Blöchl, *Physical Review B*, 1994, **50**, 17953-17979.
3. G. Kresse and D. Joubert, *Phys. Rev. B*, 1999, **59**, 1758-1775.
4. J. P. Perdew, K. Burke and M. Ernzerhof, *Phys. Rev. Lett.*, 1996, **77**, 3865-3868.
5. S. Grimme, J. Antony, S. Ehrlich and H. Krieg, *J. Chem. Phys.*, 2010, **132**, 154104.
6. J. F. Dobson and T. Gould, *J Phys Condens Matter*, 2012, **24**, 073201.
7. T. Bjorkman, A. Gulans, A. V. Krashennnikov and R. M. Nieminen, *J Phys Condens Matter*, 2012, **24**, 424218.
8. J. F. Dobson, A. White and A. Rubio, *Phys. Rev. Lett.*, 2006, **96**, 073201.
9. T. Sun, Y. Wang, H. Zhang, P. Liu and H. Zhao, *J Colloid Interface Sci*, 2015, **454**, 180-186.
10. V. Wang, N. Xu, J.-C. Liu, G. Tang and W.-T. Geng, *Computer Physics Communications*, 2021, **267**.
11. G. Henkelman and H. Jónsson, *The Journal of Chemical Physics*, 2000, **113**, 9978-9985.
12. G. Henkelman, B. P. Uberuaga and H. Jónsson, *The Journal of Chemical Physics*, 2000, **113**, 9901-9904.
13. R. N. Barnett and U. Landman, *Physical Review B*, 1993, **48**, 2081-2097.
14. K. Mathew, R. Sundararaman, K. Letchworth-Weaver, T. A. Arias and R. G. Hennig, *The Journal of Chemical Physics*, 2014, **140**, 084106.
15. K. Mathew, V. S. C. Kolluru, S. Mula, S. N. Steinmann and R. G. Hennig, *J Chem Phys*, 2019, **151**, 234101.
16. J. K. Nørskov, J. Rossmeisl, A. Logadottir, L. Lindqvist, J. R. Kitchin, T. Bligaard and H. Jónsson, *The Journal of Physical Chemistry B*, 2004, **108**, 17886-17892.
17. Á. Valdés, Z. W. Qu, G. J. Kroes, J. Rossmeisl and J. K. Nørskov, *The Journal of Physical Chemistry C*, 2008, **112**, 9872-9879.
18. Z. Duan and G. Henkelman, *ACS Catalysis*, 2019, **9**, 5567-5573.
19. Q. Wu, C. Dai, F. Meng, Y. Jiao and Z. J. Xu, *Nat Commun*, 2024, **15**, 1095.
20. J. M. P. Martirez and E. A. Carter, *J Am Chem Soc*, 2023, **145**, 12561-12575.
21. Q. Yu and J. M. Bowman, *J Phys Chem A*, 2019, **123**, 1399-1409.
22. H. Bai, D. Liu, P. Zhou, J. Feng, X. Sui, Y. Lu, H. Liu and H. Pan, *Journal of Materials Chemistry A*, 2022, **10**, 25262-25271.
23. M. Pourbaix, *NACE*, 1974, **307**.
24. H. A. Hansen, J. Rossmeisl and J. K. Nørskov, *Phys Chem Chem Phys*, 2008, **10**, 3722-3730.
25. H. A. Hansen, I. C. Man, F. Studt, F. Abild-Pedersen, T. Bligaard and J. Rossmeisl, *Phys Chem Chem Phys*, 2010, **12**, 283-290.
26. K. S. Exner, J. Anton, T. Jacob and H. Over, *Electrochimica Acta*, 2014, **120**, 460-466.
27. T. Lim, G. Y. Jung, J. H. Kim, S. O. Park, J. Park, Y. T. Kim, S. J. Kang, H. Y. Jeong, S. K. Kwak and S. H. Joo, *Nat Commun*, 2020, **11**, 412.
28. L. Ju, M. Bie, X. Tang, J. Shang and L. Kou, *ACS Appl Mater Interfaces*, 2020, **12**, 29335-29343.

29. L. Ju, J. Shang, X. Tang and L. Kou, *J Am Chem Soc*, 2020, **142**, 1492-1500.
30. Lide, D. R. CRC Handbook of Chemistry and Physics, 84th Ed.; CRC Press: Boca Raton, FL., **2003-2004**.